Research Square

Preprints are preliminary reports that have not undergone peer review.
They should not be considered conclusive, used to inform clinical practice,
or referenced by the media as validated information.

Synergistic effects of Cur-AgNPs/PSF mixed matrix membranes: enhanced separation, antibacterial, and antioxidant performance

Junhong Guo
Lanzhou University of Technology
Yongcong Yang
Lanzhou University of Technology
Xingyu Gao
Lanzhou University of Technology
Tianjing Zhao
Lanzhou University of Technology
Xuemei Bao
baoxm@lut.edu.cn
Lanzhou University of Technology

Research Article

Keywords: Polysulfone membrane, amphiphilic, Mixed matrix membrane, Antibiofouling, Antibacterial activity

Posted Date: March 24th, 2026

DOI: https://doi.org/10.21203/rs.3.rs-9139082/v1

License: This work is licensed under a Creative Commons Attribution 4.0 International License.
Read Full License

Additional Declarations: No competing interests reported.

Version of Record: A version of this preprint was published at Journal of Inorganic and Organometallic Polymers and Materials on May 15th, 2026. See the published version at https://doi.org/10.1007/s10904-026-04334-5.

Synergistic effects of Cur-AgNPs/PSF mixed matrix membranes: enhanced separation, antibacterial, and antioxidant performance

*Junhong Guo, Yongcong Yang, Xingyu Gao, Tianjing Zhao, Xuemei Bao**

College of Petrochemical Technology, Lanzhou University of Technology, Lanzhou 730050, P. R. China

*Corresponding Authors; Email: baoxm@lut.edu.cn

ABSTRACT

Curcumin-modified silver nanoparticles (Cur-AgNPs) were synthesized through a green approach and incorporated into a polysulfone (PSF) matrix to fabricate Cur-AgNPs/PSF mixed matrix membranes (**(**MMMs**)**. Subsequently, their separation, antibacterial, antibiofouling, and antioxidant characteristics were examined. The research findings demonstrated that during the nonsolvent-induced phase separation (NIPS), the hydrophilic ligand (AgNPs) of the Cur-AgNPs amphiphilic additives segregated towards the polymer/water interface, while the hydrophobic portion (Cur) was firmly anchored within the polymer matrix, leading to partial surface enrichment. The obtained Cur-AgNPs/PSF MMMs displayed uniform dispersion along with surface enrichment. Compared with the pristine PSF membrane, the Cur-AgNPs/PSF membrane demonstrated superior performance, with the pure water permeability attaining 328.9 $L \cdot m^{-2} \cdot h^{-1} \cdot bar^{-1}$ and the BSA rejection rate rising to 91.23%. The membranes also manifested favorable antibacterial activity against *Staphylococcus aureus* (*S. aureus*) and *Escherichia coli* (*E. coli*). After fouling by *S. aureus* and *E. coli*, the flux recovery ratio reached 70% - 80%, which was notably higher than that of the PSF membrane. Additionally, the Cur-AgNPs/PSF MMM displayed excellent free radical scavenging capacity. The incorporation of the amphiphilic Cur-AgNPs effectively enhanced the separation performance and antibiofouling property of PSF membranes.

Keywords: Polysulfone membrane; amphiphilic; Mixed matrix membrane; Antibiofouling; Antibacterial activity

Introduction

Freshwater availability underpins sustainable socioeconomic development. However, population growth, urbanization, and industrial expansion are increasingly intensifying the mismatch between water demand and accessible freshwater supplies[1-4]. Membrane-based separation processes, characterized by high separation efficiency, moderate energy requirements, and modular design, have been widely implemented in water purification and reuse[5-7]. Among them, ultrafiltration (UF) membranes effectively remove colloids, suspended solids, and high-molecular-weight organic matter, thereby serving as a key unit in pretreatment and advanced treatment trains. Nonetheless, UF membranes remain highly susceptible to biofouling during long-term operation[8]. Biofouling typically proceeds through initial microbial attachment, subsequent colonization, and biofilm maturation, accompanied by the secretion of extracellular polymeric substances (EPS)[9]. EPS is generally dominated by polysaccharides and proteins, and may also contain lipids and nucleic acids, which collectively enhance the cohesion, adhesion, and structural stability of the biofilm. The resulting biofilm/EPS layer aggravates pore blocking and cake-layer formation, increases hydraulic and mass-transfer resistance at the membrane interface and within pores, and promotes the transition from reversible to irreversible fouling[10]. From an operational perspective, biofouling is commonly manifested as a progressive rise in transmembrane pressure under constant-flux filtration or a decline in normalized permeability/specific flux under constant-pressure operation. These effects ultimately translate into increased energy demand, more frequent physical/chemical cleaning,

higher chemical consumption, and shortened membrane service life. Therefore, developing UF membrane materials with durable antibacterial and antibiofouling properties is critical to improve process stability and reduce maintenance costs[11].

Polysulfone (PSF), owing to its excellent mechanical strength, thermal/chemical stability, and good processability, has been extensively used as a base polymer for microfiltration and UF membranes[12-15]. To impart antibacterial functionality to PSF membranes, two major approaches have been widely explored: surface modification and bulk blending. Surface modification (e.g., coating[16], grafting[17], or in situ growth[18]) can enrich antibacterial components at the membrane surface and thus enable rapid antimicrobial responses; however, such processes are often relatively complex, and the stability of the functional layer may be compromised under long-term hydraulic shear and/or chemical cleaning. For instance, Raval et al.[19] modified PSF UF membranes with a chitosan/ZnO composite coating and reported improved separation performance together with antibacterial/antifungal activity; nevertheless, the long-term durability of the coating still warrants further verification. In contrast, blending typically disperses antibacterial fillers directly into the casting solution, followed by membrane formation via non-solvent induced phase separation (NIPS). In this case, embedding a fraction of the active component within the membrane matrix ensures long-lasting antibacterial efficacy. However, insufficient compatibility and non-uniform dispersion may cause filler aggregation and structural defects, thereby impairing permeability and selectivity. For example, Zhang et al.[20] developed guanidine-functionalized graphene/PSF MMMs that exhibited sustained antibacterial

activity while maintaining high water permeability, highlighting the potential of the blending strategy. Accordingly, improving the dispersion and interfacial stability of antibacterial fillers within polymer matrices—via surface ligands, polymer encapsulation, or surfactant-assisted regulation—remains crucial for high-performance MMMs.

Antibacterial agents for membrane applications encompass inorganic nanomaterials, organic molecules, and organic-inorganic hybrids. Among them, silver-based materials have attracted persistent attention due to their broad-spectrum antimicrobial activity. AgNPs, featuring high specific surface area and tunable surface chemistry, have been widely investigated in antimicrobial coatings[21], biomedical materials, and water-treatment-related systems[22]. Additional, AgNPs can be synthesized through physical methods[23, 24] or chemical reduction[25, 26]. In recent years, “green” synthesis routes have gained increasing interest because they minimize the use of organic solvents and strong reducing agents, offer relatively mild reaction conditions, and allow simultaneous stabilization/functionalization for improved biocompatibility. Such approaches typically employ natural products or biomass-derived compounds as reducing and stabilizing agents to couple Ag^{+} reduction with nanoparticle stabilization.

Curcumin, a natural polyphenolic compound, has been used as a green reducing/stabilizing agent for AgNPs synthesis[27]. Under alkaline conditions, Curcumin can undergo deprotonation and exhibit reductive capability to convert Ag^{+} into metallic Ag^{0}[28]; meanwhile, functional groups such as phenolic hydroxyls and

carbonyls can coordinate or interact with the Ag surface, thereby enhancing colloidal stability. In view of the inherent bioactivity of Curcumin, synergistic antibacterial and antioxidant effects can potentially be attained when Curcumin is combined with AgNPs.[29]. For example, Li et.al.[30] incorporated Curcumin and AgNPs into pectin/gelatin composite films for food packaging and reported favorable antioxidant and antimicrobial performance. These findings suggest that Curcumin-mediated green-synthesized AgNPs may provide a promising functional platform for polymeric membrane systems, enabling antimicrobial activity together with improved stability and multifunctionality.

Although the curcumin-assisted green synthesis of silver nanoparticles (AgNPs) has been verified and linked to antibacterial and antioxidant functions, polysulfone (PSF)-based antibacterial mixed matrix membranes (MMMs) have predominantly concentrated on antimicrobial performance only. Systematic investigations integrating Curcumin-mediated AgNPs into PSF membranes to simultaneously improve antibacterial, antioxidant, and antibiofouling performance are still scarce. In the present study, curcumin was utilized as both a reducing agent and a stabilizing agent, while $AgNO_3$ was employed as the silver precursor to synthesize curcumin-modified silver nanoparticles (Cur-AgNPs) through a green approach. Subsequently, their antibacterial and antioxidant properties were evaluated. Subsequently, Cur-AgNPs were incorporated into PSF casting dopes, and Cur-AgNPs/PSF mixed-matrix ultrafiltration (UF) membranes were fabricated through the non-solvent induced phase separation (NIPS) method. This research clarifies the regulatory mechanisms of Cur-AgNPs

regarding the membrane's microstructural features and interfacial characteristics. Moreover, it conducts a systematic assessment of water permeation, solute rejection, along with antibacterial, antioxidant, and antibiofouling properties. The results are anticipated to offer practical guidance for the design of long-lasting anti-biofouling ultrafiltration (UF) membranes in water reuse applications.

2.1 **Experimental Materials**

Polysulfone resin (PSF) purchased from Sigma-Aldrich Corporation. NaOH, $AgNO_3$, and Dimethylacetamide (DMAc) were purchased from Sinopharm Chemical Reagent Co., Ltd. Curcumin (Cur) was purchased from Meryer (Shanghai) Chemical Technology Co., Ltd. 1,1-diphenyl-2-picrylhydrazyl (DPPH) and 2,2′-azinobis-(3-ethylbenzothiazoline)-6 sulphonic acid (ABTS) were purchased from Tianjin Zhonglian Chemical Reagent Co., Ltd.

2.2 Preparation of Cur-AgNPs and Cur-AgNPs/PSF MMMs

Curcumin (0.5, 1.0, 1.5, and 2.0 g) was dissolved in 1.0 M NaOH to obtain alkaline curcumin solutions (NaOH-Cur) at different concentrations. All solutions were stored at low temperature in the dark to minimize curcumin degradation and ensure stability. An $AgNO_3$ solution (0.125 M) was prepared, and 1 mL of the above NaOH-Cur solution was added, upon which a rapid formation of dark particles was observed in the initially clear $AgNO_3$ solution. The mixture was stirred at 30 °C for 2 h. After reaction, the product was collected by centrifugation and washed repeatedly with deionized water to remove residual reactants. The obtained solids were dried at 50 °C to yield Cur-AgNPs

powder.

Cur-AgNPs/PSF MMMs were fabricated via the NIPS method, as illustrated in Fig. 1. A solvent system consisting of DMAc and PEG (76/8 wt%) was first prepared, followed by the addition of varying amounts of Cur-AgNPs (1, 3, 5, 7, and 9wt% relative to the total casting solution). The mixture was ultrasonicated for 30 min to ensure uniform dispersion. Subsequently, 16wt% PSF was added and stirred until completely dissolved. After degassing for 2 h to eliminate air bubbles, the homogeneous casting solution was cast onto a nonwoven fabric support using a casting knife with a gap of 400 μm at room temperature. The nascent membrane was then immediately immersed into a pure water coagulation bath to complete the phase inversion process. The prepared MMMs with different loading of Cur-AgNPs (0.1, 0.3, 0.5, 0.7 and 0.9g) are denoted as M1, M2, M3, M4 and M5, respectively, which was described in Table 1. The pristine membrane was named as PSF.

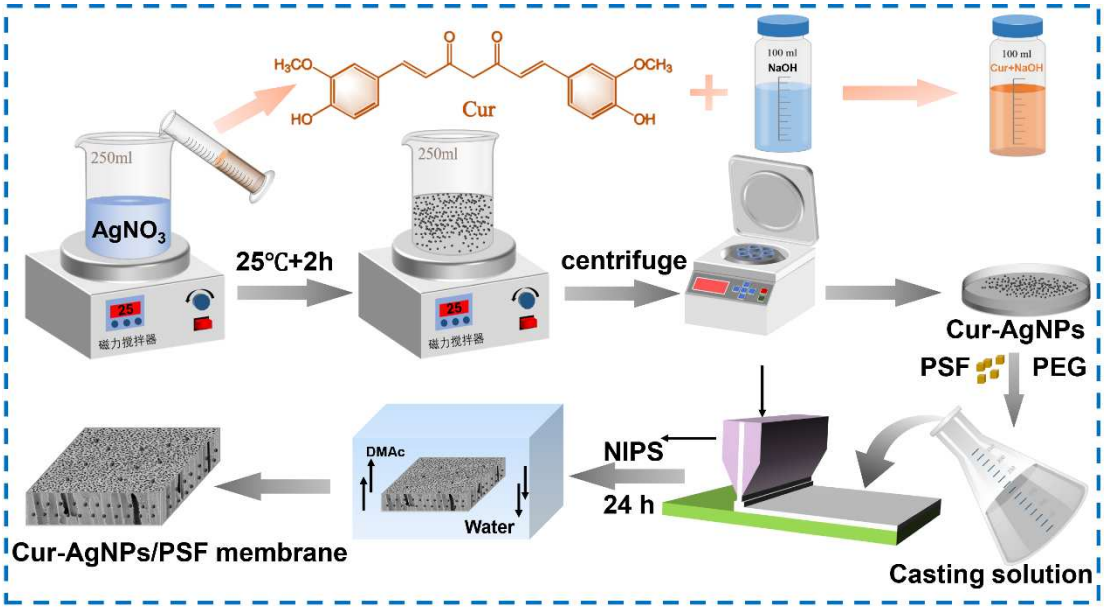


Fig. 1 Schematic illustration of Cur-AgNPs synthesis and Cur-AgNPs /PSF MMMs preparation

Table 1 Composition of Casting solution

membrane	PSF(g)	PEG(g)	DMAc(g)	Cur-AgNPs (g)
PSF	1.6	0.8	7.6	0
M1	1.6	0.8	7.6	0.1
M2	1.6	0.8	7.6	0.3
M3	1.6	0.8	7.6	0.5
M4	1.6	0.8	7.6	0.7
M5	1.6	0.8	7.6	0.9

2.3. Characterization of Cur-AgNPs and Cur-AgNPs/PSF MMMs

The chemical structure of Cur-AgNPs was characterized by Fourier transform infrared (FTIR) spectroscopy (HP300-MS-IR, JWGB Sci & Tech, China) over the range of 4000-600 cm^{-1}. X-ray diffraction (XRD) (TD-3700, Dandong Tongda, China) was employed to examine the crystalline phase over a 2θ range of 10-80°. Surface elemental composition and chemical states were analyzed by X-ray photoelectron spectroscopy (XPS). Morphological observation of Cur-AgNPs and Cur-AgNPs/PSF MMMs was performed using field-emission scanning electron microscopy (FESEM; FESEM5000, CIQTEK, China) at an accelerating voltage of 5 kV. Thermal stability was evaluated by thermogravimetric analysis (TGA; HCT-1, HENVEN, China) from 25 to 800 °C under nitrogen atmosphere (50 $mL \cdot min^{-1}$) at a heating rate of 10 $°C \cdot min^{-1}$.

2.4 Membrane filtration experiment

Measurements were performed using a terminal filter unit assembly. The effective membrane area was 13.4 cm^2, and the operating pressure was maintained at 1 bar. The process design of the filtering device is detailed in the paper[31].

The Pure-water permeance (PWP) ($L \cdot m^{-2} \cdot h^{-1} \cdot bar^{-1}$) of was calculated by

following Eq. (1)

$$PWP=\frac{V}{A\times t\times \Delta P} \quad (1)$$

where V(L) is the volume of permeated water, A (m^2) is the membrane area, t (h) is the permeation time and ΔP (bar) is the transmembrane pressure difference applied through the membrane

Bovine serum albumin (BSA) rejection tests were performed using a 0.5 g/L BSA solution in phosphate-buffered saline (PBS, pH 7.3). The BSA concentrations in the feed and permeate were measured by a UV-Vis spectrophotometer (UV-3600s, MAPADA, China) at a wavelength of 280 nm. The rejection rate was then calculated according to Eq. (2).

$$R=\frac{C_f-C_p}{C_f}\times 100\% \quad (2)$$

where C_f and C_p correspond to the BSA concentration in the feed and permeate solution, respectively. Measure its absorbance at 280 nm using a UV visible spectrophotometer and convert it into a concentration value.

2.5 Analysis of Hydrophilicity in Cur-AgNPs/PSF MMMs

Surface hydrophilicity of the membranes was assessed by static water contact angle (WCA) measurements using a contact angle analyzer (SZ-CAM, SUNZERN, China). Flat, defect-free membrane specimens were mounted on the sample stage to ensure accurate measurements by minimizing artifacts from surface curvature. At least three replicate measurements were taken at different locations on each sample in air at room temperature. The results were reported as mean ± standard deviation (SD) to

reflect both the measurement variability and the uniformity of the membrane surface.

2.6 Mechanical property analysis of Cur-AgNPs/PSF MMMs

Tensile properties of the membranes were measured using a universal testing machine (ZQ-990LB, Dongguan Zhicai, China). Rectangular specimens (3 cm × 1 cm) were cut from the membranes and conditioned under standard temperature and humidity. Tests were conducted at a constant crosshead speed, and the corresponding stress–strain curves were recorded. The tensile strength and elongation at break were derived from these curves.

2.8 Antibacterial activity of Cur-AgNPs/PSF MMMs

The antibacterial activity of Cur-AgNPs and Cur-AgNPs/PSF MMMs was evaluated against *E. coli* and *S. aureus* using an agar disk diffusion assay. Furthermore, their resistance to biofouling was assessed by quantifying the change in pure water permeance before and after bacterial contamination under simulated operating conditions.

2.9 Antioxidant activity of Cur-AgNPs/PSF MMMs

DPPH and ABTS radical-scavenging assays were employed to evaluate the antioxidant activity of Cur-AgNPs/PSF MMMs[32-34]. Membrane samples were separately immersed in the DPPH and ABTS working solutions and incubated at room temperature in the dark. For the ABTS assay, the mixture was additionally maintained under gentle stirring. The absorbance was recorded at 517 and 734 nm using a UV-vis spectrophotometer, and the radical-scavenging activity was calculated according to Eq.

(3).

$$\textit{Radical scavenging ability}\ (\%)=\left(1-\frac{A_1}{A_0}\right)\times 100 \quad (3)$$

3. Result and discussion

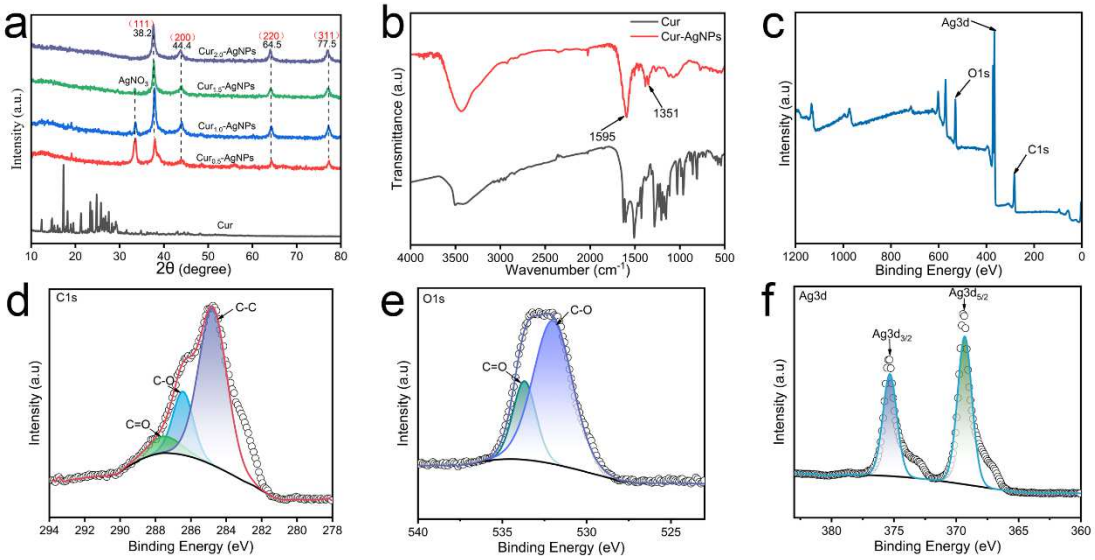
3.1 Characterization of Cur-AgNPs

X-ray diffraction was performed to examine the crystalline structure of Cur-AgNPs. The XRD patterns of Cur-AgNPs synthesized using alkaline NaOH solutions with different Curcumin amounts are shown in Fig. 2a. All samples exhibit characteristic reflections at 2θ = 38.2°, 44.4°, 64.5°, and 77.7°, which can be indexed to the (111), (200), (220), and (311) planes of metallic Ag, respectively[35]. In contrast, samples prepared with 0.5, 1.0, and 1.5 g Curcumin show an additional reflection at 2θ = 33.4°, which may be attributed to residual silver precursor or incomplete reduction of $AgNO_3$ at insufficient Curcumin dosage[28]. When the Curcumin amount was increased to 2.0 g, this extra peak was no longer observed, suggesting a more complete reduction of $AgNO_3$ under these conditions. Accordingly, 2.0 g Curcumin was selected as the optimal dosage for subsequent synthesis based on phase purity in the XRD patterns.

In addition, Cur-AgNPs were further analyzed by FTIR spectroscopy. Fig. 2b shows the FTIR spectra of pure Curcumin and Cur-AgNPs synthesized using 2.0 g Curcumin. Pure Curcumin exhibits a broad phenolic O-H stretching band at 3490 cm^{-1}[36], which shifts slightly to lower wavenumbers in Cur-AgNPs. A weak band at 2920 cm^{-1}, attributed to asymmetric C-H stretching of the methoxy group ($-OCH_3$), is

observed in both spectra[37]. The overlapping band assigned to C=C and C=O stretching shifts from 1620 cm^{-1} in curcumin to 1595 cm^{-1} in Cur-AgNPs[38]. Additionally, Cur-AgNPs exhibit a new band at 1351 cm^{-1}. These spectral shifts suggest that Ag may coordinate with the carbonyl oxygen of Curcumin, facilitating Curcumin adsorption on the nanoparticle surface and allowing Curcumin to act as a capping/stabilizing agent. Overall, the FTIR results support the successful formation of Cur-AgNPs.

X-ray photoelectron spectroscopy was also used to analyze Cur-AgNPs to obtain information on their surface elemental composition and chemical state. The XPS results are presented in Fig. 2c. Fig. 2c shows the XPS survey spectrum of Cur-AgNPs, in which the characteristic signals of C 1s, O 1s, and Ag 3d are observed. These peaks are centered at 284.8, 532.0, and 368.2 eV, respectively, in agreement with previously reported values[39, 40]. High-resolution XPS spectra of O 1s, C 1s, and Ag 3d are shown in Fig. 2d-f, respectively. The O 1s spectrum can be deconvoluted into two components at 530.2 and 531.8 eV, which are assigned to C-O and C=O species, respectively. The C 1s spectrum can be deconvoluted into three peaks at 284.8, 286.5, and 288.2 eV, corresponding to C-C/C-H, C-O, and C=O, respectively. The Ag 3d spectrum shows a characteristic spin-orbit doublet with peaks at 368.5 and 375.1 eV, assigned to Ag $3d_{5/2}$ and Ag $3d_{3/2}$, respectively, indicating the presence of metallic Ag (Ag^0)[30]. Overall, the XPS results further support the successful formation of Cur-AgNPs by revealing the expected elemental composition and chemical states.



256

257 **Fig. 2** Structural and chemical characterizations of Cur-AgNPs: (a) XRD patterns with various

258 Curcumin concentrations; (b) FTIR spectra of pristine Curcumin and as-prepared Cur-AgNPs; (c)

259 XPS survey spectrum and high-resolution spectra of (d) C 1s, (e) O 1s, and (f) Ag 3d

260 **3.2 Morphology of Cur-AgNPs and particle size distribution**

261 The morphology of the obtained Cur-AgNPs was examined by SEM, and

262 representative images are shown in Fig. 3a. SEM images reveal that the Cur-AgNPs are

263 predominantly spherical with a relatively narrow size distribution and an estimated

264 average diameter of approximately 50 nm. The particle-size analysis is in good

265 agreement with the SEM-based estimation. Nevertheless, owing to the high surface

266 energy of nanoparticles and strong van der Waals interactions, the Cur-AgNPs tend to

267 agglomerate into larger clusters. To mitigate the influence of agglomeration during

268 membrane fabrication, Cur-AgNPs were first dispersed in the solvent by ultrasonication,

269 after which PSF was added and dissolved under stirring to obtain a well-dispersed

270 casting solution.

The statistical analysis results of SEM images based on Image J software are shown in Fig. 3b. Statistics show that the average particle size of Cur-AgNPs is 43.97 nm, which is consistent with the size estimated by SEM image observation in the previous stage (about 50 nm). Nano fillers with smaller particle sizes help to form a tighter interface with the polymer matrix, significantly reducing non selective voids caused by interface defects and making the prepared composite membrane structure denser. In addition, the high specific surface area characteristics of nanoparticles enable them to achieve higher efficiency and less dosage when endowing PSF polymer matrix with efficient antibacterial properties. This characteristic is of great significance for achieving surface functionalization modification of matrix materials while maintaining their intrinsic properties.

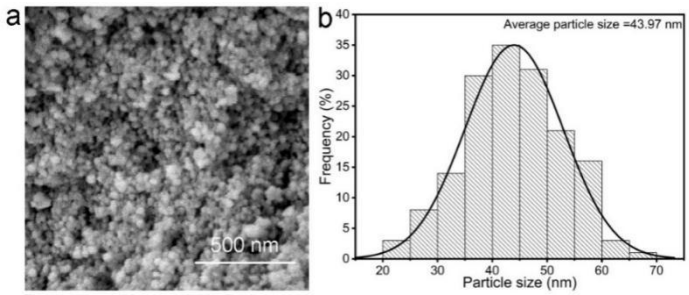


Fig. 3 SEM image (a) and particle size distribution (b) of the synthesized Cur-AgNPs

3.3 Thermal stability of Cur-AgNPs

Thermal stability of Cur-AgNPs was evaluated by TGA, as shown in Fig. 4a. Pure Curcumin shows its major mass loss in the range of 200-400 °C, which can be attributed to the decomposition of labile functional groups. Above 400 °C, Curcumin undergoes further thermal decomposition and carbonization, leaving a residual mass of approximately 40% at 800 °C[41, 42]. In contrast, Cur-AgNPs exhibit enhanced

thermal stability. From 25 to 500 °C, Cur-AgNPs display a gradual mass loss, indicating progressive thermal decomposition, whereas the mass remains relatively stable between 500 and 800 °C, yielding a residual mass of approximately 80% at 800 °C. The markedly higher residual mass suggests improved thermal stability of Cur-AgNPs. This enhancement may be attributed to interactions between Ag nanoparticles and Curcumin, which can restrict molecular mobility and delay thermal decomposition. Such stability is advantageous for subsequent membrane fabrication and applications involving thermal treatment. The DTG curve of Cur-AgNPs（Fig. 4b）remained nearly horizontal throughout the heating process, indicating its excellent thermal stability and the absence of volatile impurities. This characteristic allows Cur-AgNPs to serve as stable inorganic anchors within the PSF matrix, effectively shifting the decomposition temperature of the resulting MMMs.

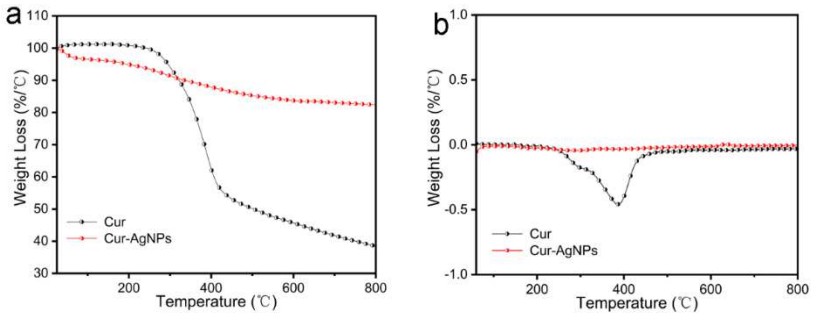


Fig. 4 TG (a) and DTG (b) curves of Cur and Cur-AgNPs

3.4 Antibacterial activity of Cur-AgNPs

Used agar plate diffusion method to determine their inhibitory activity against *S. aureus* and *E. coli*. Fig. 5 shows the corresponding inhibition zone results, where a and b are the inhibition zone photos of Cur-AgNPs against *S. aureus* and *E. coli*, respectively. It can be observed that Cur-AgNPs have significant inhibitory effects on

both bacteria, forming clear inhibition zones. At the same dosage of Cur-AgNPs, their inhibition zone against *S. aureus* was slightly larger than that against *E. coli*, which may be related to the different external structures of the two bacterial cells. The main external barrier of *S. aureus* is a thick and porous peptidoglycan layer, which can be easily penetrated by AgNPs; The outer membrane of *E. coli* is a dense and asymmetric phospholipid bilayer structure, which has a strong blocking effect on antibacterial components, resulting in a slower penetration rate and relatively smaller size of the antibacterial zone[43]. The antibacterial effect of Cur-AgNPs mainly comes from the bactericidal mechanism of AgNPs themselves, and Curcumin also has certain antibacterial activity. The synergistic effect of the two endows Cur-AgNPs with good antibacterial performance. Specifically, AgNPs can slowly release Ag^{+}, which can disrupt the integrity of bacterial cell walls and membranes, causing physical damage; In addition, Ag^{+} can further penetrate into bacterial cells, interfere with cellular metabolic processes, disrupt DNA replication, and induce the generation of reactive oxygen species (ROS), ultimately leading to bacterial death[44].

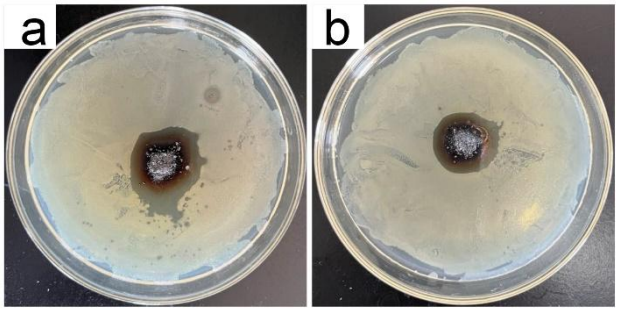


Fig. 5 Digital photographs of inhibition zones of Cur-AgNPs against *S. aureus* (a) and *E. coli* (b)

3.4 Morphology of PSF and Cur-AgNPs /PSF MMMs

Fig. 6 shows the surface and cross-sectional SEM morphologies of the pristine

PSF membrane and Cur-AgNPs/PSF MMMs prepared with different Cur-AgNPs loadings. Compared with the pristine PSF (Fig. 6a), the membrane surfaces become smoother and denser at Cur-AgNPs loadings of 1, 3, and 5wt% (Fig. 6b-d), with surface pores markedly reduced and in some regions less discernible. This behavior may be attributed to the migration and enrichment of Cur-AgNPs toward the membrane-coagulation bath interface during phase inversion[45], leading to a denser near-surface region that partially masks surface pores; consistently, the Pure Water Permeance(PWP) decreases at low Cur-AgNPs loadings (1-5wt%). When the Cur-AgNPs loading was increased to 7 and 9wt% (Fig. 6e, f), nanoparticle enrichment on the membrane surface became more pronounced and was clearly visible. Under these conditions, the PWP of the Cur-AgNPs/PSF MMMs (M4 and M5) is improved relative to that of the PSF membrane. This enhancement is attributed to the enrichment of Cur-AgNPs on the membrane surface, which increases the surface hydrophilicity, promotes the adsorption and transport of water molecules through the membrane matrix, and consequently reduces permeation resistance, leading to an elevated PWP. Cross-sectional SEM images indicate a relatively uniform distribution of Cur-AgNPs throughout the membrane, with no obvious large-scale agglomeration. Compared with pristine PSF featuring smooth pore walls, numerous particle-like features are observed attached to or embedded within pore walls of the MMMs, suggesting good interfacial adhesion between Cur-AgNPs and the PSF matrix. Such a hierarchical distribution may enable surface-bulk functional synergy: surface-enriched Cur-AgNPs can contribute to a functionalized near-surface region and enhance contact antibacterial activity, while

nanoparticles dispersed within the porous sublayer may help stabilize the pore architecture and improve separation performance, thereby contributing to a balanced permeance-selectivity-antibacterial profile.

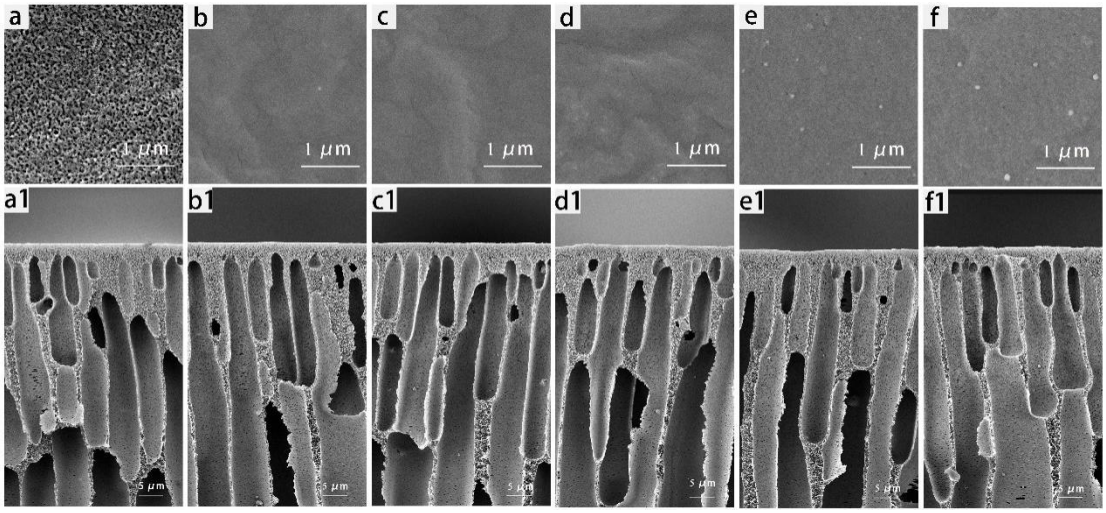


Fig. 6 SEM images of the surface and cross-section morphology of PSF membrane (a, a1) and Cur-AgNPs/PSF MMMs M1-M5 (b, b1 to f, f1)

3.5 Characterization of Cur-AgNPs /PSF MMMs

Fig. 7a shows the XRD patterns of PSF and Cur-AgNPs/PSF MMMs prepared with different Cur-AgNPs loadings. All Cur-AgNPs/PSF MMMs exhibit distinct diffraction peaks at identical 2θ positions, and the peak intensities increase progressively with increasing Cur-AgNPs loading. These reflections at 2θ = 38.3°, 44.5°, 64.65°, and 77.7° can be indexed to the (111), (200), (220), and (311) planes of face-centered cubic Ag[46], respectively. Collectively, these results indicate that Cur-AgNPs are successfully incorporated into the PSF matrix and that the crystalline structure of Ag is retained after membrane fabrication.

XPS was used to analyze the surface elemental composition of pristine PSF and

Cur-AgNPs/PSF MMMs, as shown in Fig. 7b. Fig. 7b presents the XPS survey spectra of pristine PSF and Cur-AgNPs/PSF MMMs. Compared with pristine PSF, the Cur-AgNPs/PSF MMMs exhibit an additional signal at 368.2 eV, attributable to the Ag 3d region from Cur-AgNPs. The binding energies of S 2p, C 1s, and O 1s are consistent with reported values[47], with no appreciable shift observed after Cur-AgNPs incorporation. Fig. 7c shows the high-resolution Ag 3d spectrum, displaying the characteristic spin–orbit doublet (Ag $3d_{5/2}$ and Ag $3d_{3/2}$) at binding energies consistent with metallic Ag[39, 40]. Overall, the XPS results support the successful incorporation of Cur-AgNPs and their retention at the surface of the PSF-based MMMs.

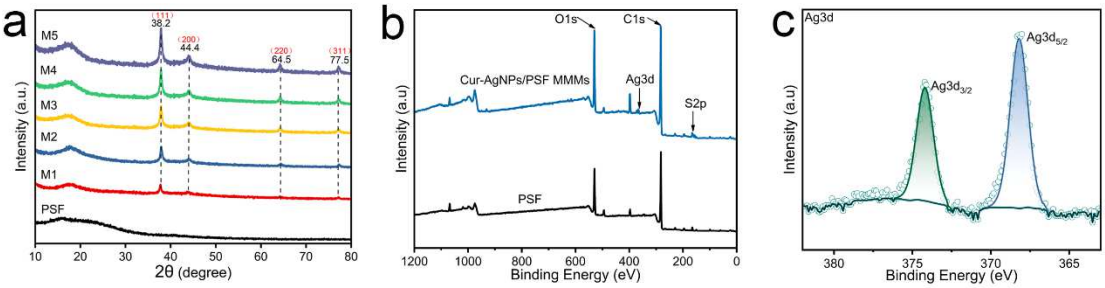


Fig. 7 XRD patterns (a), XPS survey spectra (b) of PSF membrane and Cur-AgNPs/PSF MMMs, and high-resolution XPS spectrum of Ag 3d (c)

3.6 Thermal stability and mechanical properties of Cur-AgNPs /PSF MMMs

TGA was performed for PSF membrane and Cur-AgNPs/PSF MMMs with different Cur-AgNPs loadings, as shown in Fig. 8. Fig. 8a shows the TG curves, where all membranes exhibit a similar two-step mass-loss profile: a minor mass loss below 450 °C, mainly due to the removal of absorbed water and residual solvent, followed by rapid mass loss between 450 and 550 °C associated with thermal degradation of the PSF backbone[48]. Compared with pristine PSF, the Cur-AgNPs/PSF MMMs exhibit a higher residual mass at 800 °C (char yield), which increases from 38% for PSF to 42.5%

for M1 and to 59% for M5. This trend suggests improved thermal stability upon Cur-AgNPs incorporation, likely due to the intrinsic thermal stability of Cur-AgNPs and interfacial interactions that restrict PSF chain mobility and delay decomposition[49]. Fig. 8b shows the DTG curves, where T_{max} corresponds to the maximum mass-loss rate. T_{max} increases from 525 °C for pristine PSF to 534 °C for M5, further supporting enhanced thermal resistance of the composite membranes. Such thermal robustness is beneficial for membrane fabrication and potential applications involving elevated-temperature operation.

Tensile properties of PSF membrane and Cur-AgNPs/PSF MMMs with different Cur-AgNPs loadings were evaluated, as shown in Fig. 8. Fig. 8c shows the representative stress-strain curves. The PSF membrane exhibits a tensile strength of 3.21 MPa and elongation at break of 21.96%. Upon incorporation of Cur-AgNPs, the mechanical response changed notably: for M1 (1wt%), tensile strength increased to 3.91 MPa and elongation at break increased to 27.69%. For M2 (3wt%), the tensile strength further increased to 4.01 MPa while maintaining a relatively high elongation at break (25.68%). When the loading increased to 5wt% (M3), both tensile strength and elongation at break decreased to 3.66 MPa and 24.40%, respectively, suggesting an optimum Cur-AgNPs loading of approximately 3wt%. At low loadings, well-dispersed nanoparticles may reinforce the matrix by promoting stress transfer and strengthening interfacial interactions, whereas at higher loadings, nanoparticle aggregation and interfacial defects may act as stress concentrators and weaken interfacial adhesion, leading to deteriorated mechanical performance[50]. Consistently, further increases in

loading (M4-M5) led to a continued decline; for M4, tensile strength decreased to 3.10 MPa and elongation at break 24.65%. Fig. 8d summarizes tensile strength and elongation at break, further illustrating the dependence of mechanical properties on Cur-AgNPs loading. Overall, moderate Cur-AgNPs incorporation can enhance the mechanical performance of the MMMs, whereas excessive loading may cause deterioration; therefore, optimizing nanofiller loading is essential for achieving high-performance composite membranes[51].

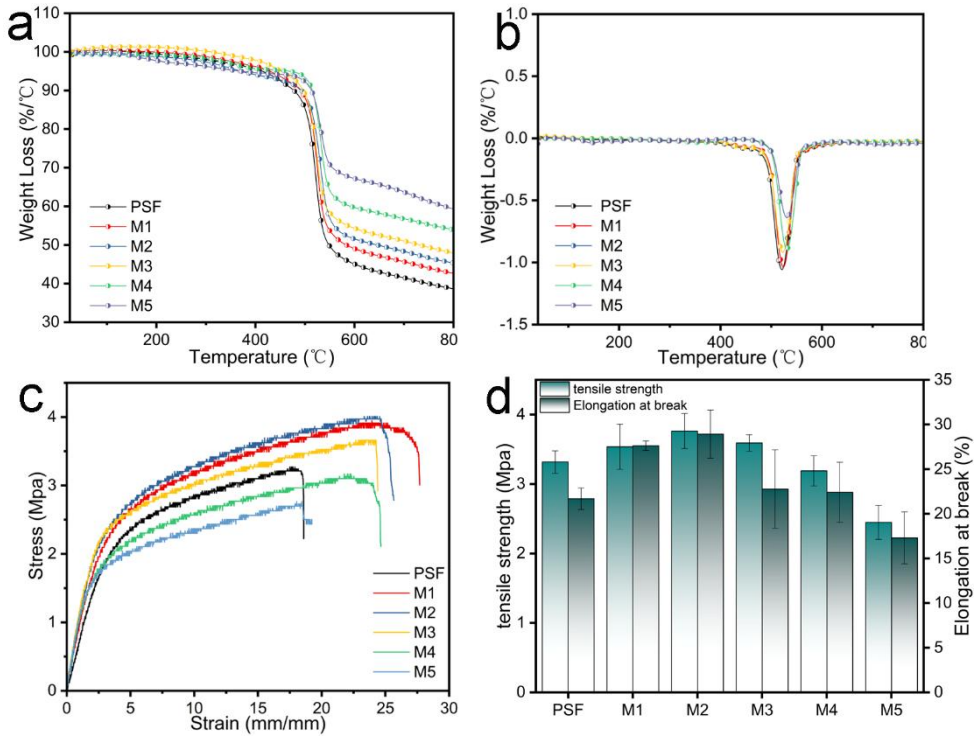


Fig. 8 Thermal and mechanical properties of the pristine PSF and Cur-AgNPs/PSF MMMs: (a) TGA and (b) DTG profiles; (c) representative tensile stress-strain curves; (d) tensile strength and elongation at break

3.7 The viscosity of the casting solution and the hydrophilicity of Cur-AgNPs /PSF MMMs

The rheological behavior of the casting solutions is illustrated in Fig. 9a. The pristine PSF solution exhibited a viscosity of 354.3 mPa·s, whereas the viscosity of the hybrid systems increased monotonically to 468.3 mPa·s upon the incorporation of Cur-AgNPs. The small size and superior colloidal stability of Cur-AgNPs within the PSF matrix are pivotal in modulating the physical characteristics of the MMMs. A highly homogenized dispersion is conducive to fabricating a coherent and defect-free selective layer, which is instrumental in improving both the mechanical integrity and separation performance[52]. Moreover, the robust interfacial interactions between the Cur-AgNPs and the PSF segments significantly restrict the segmental mobility of the polymer chains. This increased internal friction and steric hindrance effectively hinder the fluidic transition, resulting in the observed macroscale elevation in dope viscosity[53].

WCA measurements (Fig. 9b) were used to assess the surface wettability of PSF membrane and Cur-AgNPs/PSF MMMs. The WCA decreased from 83.8° for pristine PSF to 75.66° for M5, indicating an improvement in surface hydrophilicity after Cur-AgNPs incorporation. The observed enhancement in membrane hydrophilicity is primarily attributed to an interfacial segregation mechanism. Curcumin molecules contain polar functional groups, such as -OH and -OCH_3, which possess strong hydrogen-bonding capability and higher intrinsic polarity than the polymer matrix. During membrane formation, these polar moieties tend to migrate toward the membrane–air interface to minimize interfacial free energy, leading to surface enrichment of hydrophilic groups and consequently increasing surface polarity and wettability. Similar phenomena have been reported for other small-molecule modifiers;

for instance, studies employing riboflavin as a functional additive have demonstrated that the intrinsic polarity and molecular structure of such additives can significantly modify the surface free energy and wetting behavior of polymer membranes[54]. In addition, Ag nanoparticles may increase the surface energy and provide additional sites that facilitate water-surface interactions[55]. Changes in the near-surface pore structure and roughness induced by Cur-AgNPs incorporation may also contribute to the observed wettability behavior. Nevertheless, the overall reduction in WCA is moderate, likely because the number of available -OH groups in curcumin is relatively limited and some functional sites may participate in coordination with Ag, reducing the density of free hydrophilic groups.

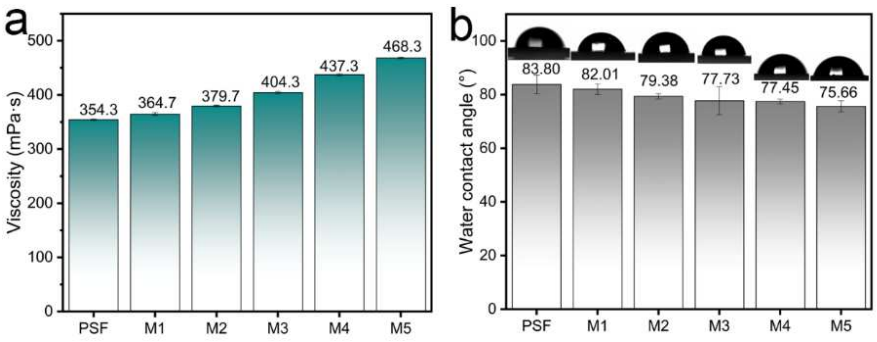


Fig. 9 Viscosity of the casting solutions (a) and water contact angles (b) of the PSF membeanes and Cur-AgNPs/PSF MMMs

3.8 PWP and BSA rejection of Cur-AgNPs /PSF MMMs.

Fig. 10 summarizes the PWP and BSA rejection of PSF membranes and CurAgNPs/PSF MMMs prepared with different Cur-AgNPs loadings. PSF exhibited a PWP of 282.84 $L \cdot m^{-2} \cdot h^{-1} \cdot bar^{-1}$ and a BSA rejection of 80.02%. At low loadings (M1, 1wt%; M2, 3wt%), BSA rejection increased to 97.53% and 96.75%, respectively,

indicating enhanced selectivity; meanwhile, the pure-water permeance decreased, consistent with the formation of a denser near-surface (skin) layer observed by SEM. With further increases in Cur-AgNPs loading, BSA rejection showed a slight downward trend, whereas pure-water permeance increased markedly. At higher loadings (M4, 7wt%; M5, 9wt%), the pure-water permeance increased to 328.92 and 319.16 $L \cdot m^{-2} \cdot h^{-1} \cdot bar^{-1}$, respectively, while BSA rejection remained above 91%. This improvement is attributed to changes in membrane structure and surface hydrophilicity: at higher addition levels, the dispersed nanoparticles promote the formation of more interconnected pores within the membrane, facilitating water permeation. Meanwhile, the enhanced surface hydrophilicity further contributes to the increased flux. Overall, M4 (7wt% Cur-AgNPs) delivered the best permeance–rejection trade-off, with a pure-water permeance of 328.92 $L \cdot m^{-2} \cdot h^{-1} \cdot bar^{-1}$ and a BSA rejection of 91.23%. Based on this balance, M4 was selected for subsequent antibacterial evaluations as a representative membrane offering both favorable separation performance and functional activity.

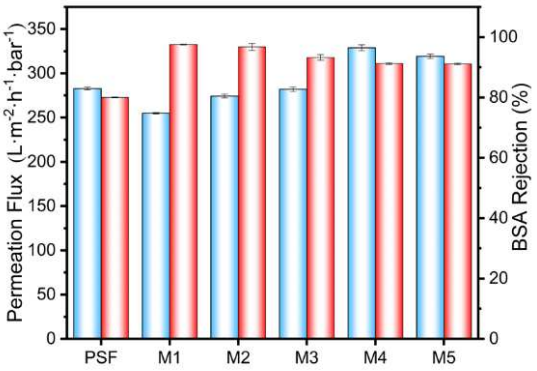


Fig. 10 PWP and BSA rejection of the PSF and Cur-AgNPs/PSF MMMs

3.9 Antibacterial activity of Cur-AgNPs /PSF MMMs

Antibacterial activity of the membrane samples (M1-M5) with different Cur-AgNPs loadings was evaluated against *E. coli* and *S. aureus* using the agar disk diffusion assay, and the results are shown in Fig. 11. In Fig. 11, panels a-e show photographs of inhibition zones for M1-M5 against *S. aureus*, while panels a1-e1 correspond to *E. coli*. With increasing Cur-AgNPs loading, the inhibition zones increased from negligible/absent to clearly discernible for both strains. At the same loading, the inhibition zones against *S. aureus* were larger than those against *E. coli*, suggesting a more pronounced inhibitory effect toward *S. aureus*. This difference may be related to the intrinsic structural disparity between Gram-positive and Gram-negative bacteria; *E. coli* (Gram-negative) typically exhibits lower susceptibility due to the protective outer membrane barrier that can impede the interaction and/or diffusion of antibacterial species. The antibacterial activity of Cur-AgNPs/PSF MMMs originates from the incorporated Cur-AgNPs. Both curcumin and silver nanoparticles possess intrinsic antibacterial properties, and their enrichment on the membrane surface enhances contact-based bacterial inactivation. Through their synergistic action, the Cur-AgNPs/PSF MMMs achieve excellent overall antibacterial performance, with AgNPs considered the primary antibacterial component. In aqueous/biological media, AgNPs may release diffusible silver species (e.g., Ag^{+}), which can contribute to the observed inhibition zones[56]. Overall, these results demonstrate that the antibacterial performance of Cur-AgNPs/PSF MMMs can be tuned by adjusting the Cur-AgNP loading.

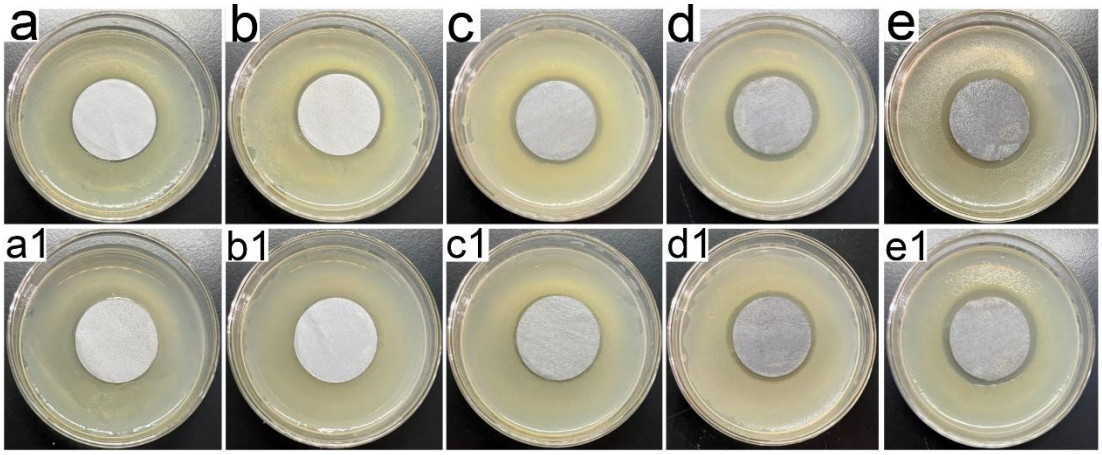


Fig. 11 Digital photographs of inhibition zones of Cur-AgNPs/PSF MMMs M1-M5 against *S. aureus* (a-e) and *E. coli* (a1-e1)

3.9 biofouling resistance of Cur-AgNPs /PSF MMMs.

Changes in PWP of PSF and the optimally loaded Cur-AgNPs/PSF MMMs (M4) before and after bacterial contamination were compared, as shown in Fig. 12. The data show that permeance decreased for both membranes after contamination, with a markedly different extent of decline. For *E. coli* contamination, PSF membranes decreased from 293.03 to 164.75 $L \cdot m^{-2} \cdot h^{-1} \cdot bar^{-1}$, corresponding to a permeance retention of 56.22%, whereas M4 decreased from 340.12 to 253.09 $L \cdot m^{-2} \cdot h^{-1} \cdot bar^{-1}$ (74.41% retention). For *S. aureus* contamination, PSF membranes decreased from 305.58 to 167.74 $L \cdot m^{-2} \cdot h^{-1} \cdot bar^{-1}$ (54.89% retention), while M4 decreased from 356.21 to 273.20 $L \cdot m^{-2} \cdot h^{-1} \cdot bar^{-1}$, corresponding to a retention of 76.70%. The observed differences may be attributed to the distinct antibacterial activities of the membrane surfaces. PSF membranes lacks intrinsic antibacterial activity, allowing bacteria to readily adhere and proliferate, which promotes biofilm formation, increases hydraulic resistance, and consequently reduces permeance after contamination[57]. In contrast,

M4 contains relatively well-dispersed Cur-AgNPs, which may gradually release Ag^{+} and suppress bacterial activity, thereby delaying biofilm development and maintaining permeance retention above 70% after contamination.

Overall, the Cur-AgNPs/PSF MMMs exhibit pronounced antibacterial activity and mitigate permeance attenuation induced by bacterial fouling, thereby maintaining more stable separation performance under contamination conditions. These attributes highlight their potential for water-treatment applications where biofouling is prevalent, such as wastewater purification and bioseparations.

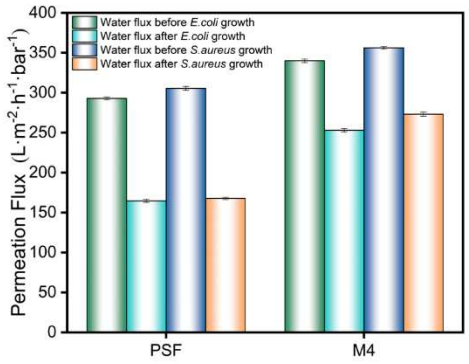
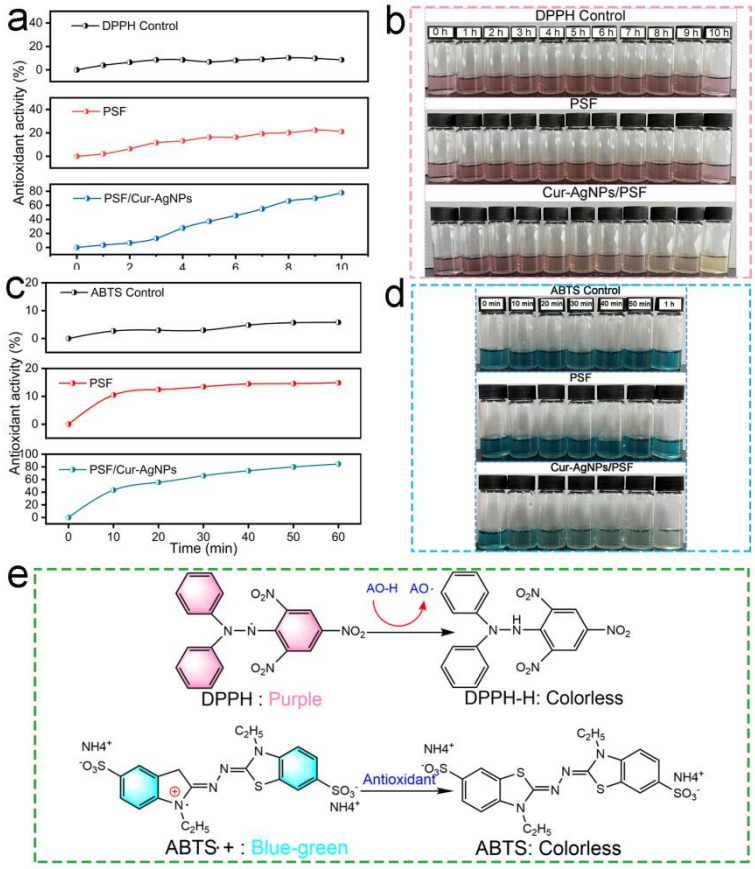


Fig. 12 changes in PWP of the PSF and M4 before and after biofouling

3.11 Antioxidant activity of Cur-AgNPs /PSF MMMs

The antioxidant activity of Cur-AgNPs/PSF MMMs was assessed using DPPH and ABTS radical-scavenging assays, with a blank (no membrane) and PSF membranes as controls (Fig. 13). Fig. 13a shows the time-dependent DPPH scavenging efficiency. After 10 h at the same initial radical concentration, the DPPH scavenging efficiencies were 8.58% for the blank and 21.03% for PSF membranes, which may be associated with nonspecific adsorption and/or background radical consumption in the presence of

534 the polymer membrane. In contrast, M4 achieved a DPPH scavenging efficiency of
535 77.92%. Photographs of the DPPH· solution (Fig. 13b) visually corroborate these
536 results: the blank and PSF groups exhibited only limited color fading (purple/red),
537 whereas the M4-containing solution gradually decolorized to pale yellow. This behavior
538 may be attributed to hydrogen-atom donation from phenolic -OH groups in curcumin,
539 while AgNPs may also contribute to radical quenching, and the combined presence of
540 curcumin and AgNPs likely accounts for the markedly enhanced antioxidant
541 response[58, 59]. Similarly, Fig. 13c shows that ABTS scavenging after 1 h increased
542 from 5.79% (blank) and 14.87% (PSF) to 84.53% (M4), consistent with the pronounced
543 decolorization observed in Fig. 13d. Overall, Cur-AgNPs/PSF MMMs show strong
544 radical-scavenging activity in both assays, indicating that Cur-AgNPs incorporation can
545 impart antioxidant functionality to PSF-based membranes[60]. The underlying
546 antioxidant mechanism is depicted in Fig. 13e. The Cur-AgNPs/PSF MMMs exhibit
547 potent radical scavenging activity, where the active phenolic groups of Curcumin act as
548 hydrogen donors (H·) to stabilize the DPPH radical, triggering a characteristic color
549 transition from purple to yellow. Similarly, when the M4 membrane is introduced into
550 the $ABTS^{\cdot+}$cationic radical system, the Curcumin-based functional sites facilitate the
551 transfer of electrons or hydrogen atoms. This leads to the reduction of the bluish-green
552 $ABTS^{\cdot+}$ into its neutral, colorless ABTS form, resulting in a significant decrease in
553 optical density as the radicals are quenched[61, 62].



554

555 **Fig. 13** Antioxidant properties and proposed mechanism of Cur-AgNPs/PSF MMMs: (a, c) DPPH

556 and ABTS radical scavenging efficiency; (b, d) digital photographs of the corresponding radical

557 solutions; (e) schematic illustration of the antioxidant mechanism

558 **Conclusion**

559 Cur-AgNPs were synthesized via a green route and incorporated into a PSF matrix

560 to fabricate Cur-AgNPs/PSF MMMs. At an optimal Cur dosage of 2.0 g, the obtained

561 nanoparticles exhibited uniform size distribution (approximately 44 nm) and a well-

562 defined crystalline structure. During membrane formation via phase inversion, the

563 surface enrichment of Cur-AgNPs occurred, driven by interfacial energy minimization.

564 π-π interactions between Cur and the PSF matrix facilitated nanoparticle migration,

565 while rapid solvent-non-solvent exchange convectively transported the nanoparticles

toward the membrane surface, resulting in enhanced hydrophilicity and permeability.

The incorporation of Cur-AgNPs significantly improved the physicochemical properties of the Cur-AgNPs/PSF MMMs. At an optimal loading of 7wt%, the membranes maintained structural integrity while exhibiting enhanced thermal stability (residual char yield of 59% and T_{max} of 534°C), increased tensile strength (up to 4.01 MPa), and improved surface hydrophilicity. The Cur-AgNPs/PSF MMMs demonstrated pronounced antibacterial activity against both *S. aureus* and *E. coli*, effectively suppressing bacterial proliferation and mitigating biofouling. After dynamic fouling tests, the membranes retained 70-80% of their initial water flux, indicating robust antifouling capacity. Furthermore, owing to the synergistic antioxidant effects of curcumin and silver nanoparticles, the membranes exhibited notable radical scavenging activity, with DPPH and ABTS scavenging efficiencies of 77.92% and 84.53%, respectively.

In summary, the developed Cur-AgNPs/PSF MMMs integrate enhanced mechanical properties, improved thermal stability, sustained antibacterial functionality, and efficient antioxidant capability, demonstrating considerable potential for applications in advanced water treatment, bioseparation, and antifouling membranes. Future work should focus on optimizing nanofiller dispersion and evaluating long-term operational stability to facilitate practical deployment.

CRediT authorship contribution statement

Yongcong Yang: Formal analysis, Investigation, Validation, Visualization,

Writing – original draft, Writing – review & editing. **Tianjing Zhao**: Investigation, Validation. **Xingyu Gao**: Investigation, Validation. **Junhong Guo**: Investigation, Writing – review & editing. **Xuemei Bao**: Conceptualization, Supervision, Writing – review & editing.

Declaration of competing interest

The authors declare that they have no known competing financial interests or personal relationships that could have appeared to influence the work reported in this paper.

Acknowledgements

This work was financially supported by National Natural Science Foundation of China(U24A20533).

References

1. C. He, Z. Liu, J. Wu, X. Pan, Z. Fang, J. Li, and B. A. Bryan, Nat Commun.**12**, 4667(2021)
2. J. Cai, X.-L. Cao, Y. Zhao, F.-Y. Zhou, Z. Cui, Y. Wang, and S.-P. Sun, J. Membr. Sci.**600**, 117863(2020)
3. J. Yin and B. Deng, J. Membr. Sci.**479**, 256-275(2015)
4. A. Sunil, M. S. Gopika, S. Jayasudha, and P. B. Nair, J. Inorg. Organomet. Polym. Mater., (2025)
5. K. J. H. A. M. M. CLARK, Environ. Sci. Technol.**36**, 3571-3576(2002)
6. P. S. Goh, B. C. Ng, W. J. Lau, and A. F. Ismail, Sep. Purif. Rev.**44**, 216-249(2014)
7. X. Bao, Y. Yang, T. Zhao, S. Liu, W. Zhou, Q. Liu, F. Yu, and Y. Yang, J. Inorg. Organomet. Polym. Mater.**35**, 5315-5325(2025)
8. S.-H. Park, S. H. Kim, S.-J. Park, S. Ryoo, K. Woo, J. S. Lee, T.-S. Kim, H.-D. Park, H. Park, Y.-I. Park, J. Cho, and J.-H. Lee, J. Membr. Sci.**513**, 226-235(2016)
9. Y.-J. Gao, R.-N. Wang, Y. Hong, and Y.-H. Wu, Water Cycle.**6**, 254-258(2025)
10. A. Ramesh, D. J. Lee, M. L. Wang, J. P. Hsu, R. S. Juang, K. J. Hwang, J. C. Liu, and S. J. Tseng, Sep. Sci. Technol.**41**, 1345-1370(2006)

11. X. Zhao, R. Zhang, Y. Liu, M. He, Y. Su, C. Gao, and Z. Jiang, J. Membr. Sci. .**551**, 145-171(2018)
12. S. Zhang, J. Zhou, Z. Wang, J. Xia, and Y. Wang, Front. Chem. Sci. Eng.**16**, 745-754(2021)
13. N. A. Alenazi, M. A. Hussein, K. A. Alamry, and A. M. Asiri, Des. Monomers Polym.**20**, 532-546(2017)
14. Y. Kang, M. Obaid, J. Jang, M.-H. Ham, and I. S. Kim, Chemosphere.**207**, 581-589(2018)
15. S. C. Mamah, P. S. Goh, A. F. Ismail, N. D. Suzaimi, L. T. Yogarathinam, Y. O. Raji, and T. H. El-badawy, J. Water Process Eng.**40**, 101835(2021)
16. Y. Zhao, Y. Zhang, F. Li, Y. Bai, Y. Pan, J. Ma, S. Zhang, and L. Shao, J. Membr. Sci.**627**, 119234(2021)
17. P. Suresh, M. M. Sibley, A. C. Che, L. M. Ward, S. T. Weinman, and C. E. Duval, J. Membr. Sci.**731**, 124243(2025)
18. D. Han, H. Liu, H. Chen, X. Hu, Y. Jia, C. Wu, and L. wang, J. Membr. Sci.**741**, (2026)
19. S. Liu, Y. Zhao, M. Xu, J. Wen, H. Wang, H. Yan, X. Gao, B. Niu, and W. Li, Int. J. Biol. Macromol.**256**, 128014(2024)
20. J. Zhang, Y. n. Xu, S. Chen, J. Li, W. Han, X. Sun, D. Wu, Z. Hu, and L. Wang, Appl. Surf. Sci.**434**, 806-815(2018)
21. K.W. Lem1, A. Choudhury2, A.A. Lakhani2, P. Kuyate2, J.R. Haw3, D.S. Lee4, Z. Iqbal5 and C.J. Brumlik2,*, Recent Patents on Nanotechnology.**6**, 60-72(2012)
22. T. Bruna, F. Maldonado-Bravo, P. Jara, and N. Caro, Int. J. Mol. Sci.**22**, 7202(2021)
23. A. P. Reverberi, M. Vocciante, M. Salerno, M. Ferretti, and B. Fabiano, Materials.**13**, 63(2019)
24. R. Radičić, D. Maletić, D. Blažeka, J. Car, and N. Krstulović, Nanomaterials.**12**, 3484(2022)
25. C. Quintero-Quiroz, N. Acevedo, J. Zapata-Giraldo, L. E. Botero, J. Quintero, D. Zárate-Triviño, J. Saldarriaga, and V. Z. Pérez, Biomaterials Research.**23**, (2019)
26. D. T. Thuc, T. Q. Huy, L. H. Hoang, B. C. Tien, P. Van Chung, N. T. Thuy, and A.-T. Le, Mater. Lett.**181**, 173-177(2016)
27. D. Zheng, C. Huang, H. Huang, Y. Zhao, M. R. U. Khan, H. Zhao, and L. Huang, Chemistry & Biodiversity.**17**, e2000171(2020)
28. M. J. Khan, K. Shameli, A. Q. Sazili, J. Selamat, and S. Kumari, Molecules.**24**, 719(2019)
29. M. Cacciari, **45**, 13-22(2005)
30. M. E. Mahmoud, M. F. Amira, M. E. Abouelanwar, and M. Abdel Salam, J. Environ. Chem. Eng.**9**, 104697(2021)
31. X. Bao, F. Wang, Q. Liu, F. Yu, and Y. Yang, Colloids and Surfaces A: Physicochemical and Engineering Aspects.**641**, 128568(2022)
32. S. Mao, Y. Ren, C. Wei, S. Chen, X. Ye, and T. Jinhu, Food Hydrocolloids.**145**, 109032(2023)
33. A. Floegel, D.-O. Kim, S.-J. Chung, S. I. Koo, and O. K. Chun, Journal of Food Composition and Analysis.**24**, 1043-1048(2011)

34. J. Niu, G. Xu, S. Jiang, H. Li, and G. Yuan, Int. J. Biol. Macromol.**94**, 154-160(2017)
35. V. Subha, A. Ranu, A. Shankar, S. Kirubanandan, E. Satheeshkumar, S. Suresh, A. Pugazhendhi, and R. Ilangovan, Prog. Org. Coat.**166**, 106782(2022)
36. K. Sindhu, A. Rajaram, K. J. Sreeram, and R. Rajaram, RSC Advances.**4**, 1808-1818(2014)
37. A. D. Verma, N. Jain, S. K. Singha, M. A. Quraishi, and I. Sinha, Journal of Chemical Sciences.**128**, 1871-1878(2016)
38. R. S. Pandit, S. C. Gaikwad, G. A. Agarkar, A. K. Gade, and M. Rai, 3 Biotech.**5**, 991-997(2015)
39. G. Moradi, S. Zinadini, L. Rajabi, and A. Ashraf Derakhshan, Chem. Eng. J.**390**, 124546(2020)
40. M. A. Abdelwahab, A. Nabil, H. El-Hosainy, R. Tahway, and M. S. Taha, Results in Chemistry.**7**, 101274(2024)
41. O. Nasrallah, R. El Kurdi, M. Mouslmani, and D. Patra, Curr. Nanomater.**3**, 147-152(2019)
42. S. Ravindra, A. F. Mulaba-Bafubiandi, V. Rajinikanth, K. Varaprasad, N. Narayana Reddy, and K. Mohana Raju, J. Inorg. Organomet. Polym. Mater.**22**, 1254-1262(2012)
43. B. Li, X. Li, H. Lin, and Y. Zhou, BioMed Research International.**2018**, 1-11(2018)
44. B. Le Ouay and F. Stellacci, Nano Today.**10**, 339-354(2015)
45. N. Alnairat, M. Abu Dalo, R. Abu-Zurayk, S. Abu Mallouh, F. Odeh, and A. Al Bawab, Polymers.**13**, (2021)
46. P. F. Andrade, A. F. de Faria, S. R. Oliveira, M. A. Z. Arruda, and M. d. C. Gonçalves, Water Res.**81**, 333-342(2015)
47. M. Hu, Z. Cui, J. Li, L. Zhang, Y. Mo, D. S. Dlamini, H. Wang, B. He, J. Li, and H. Matsuyama, J. Colloid Interface Sci.**552**, 319-331(2019)
48. M. Ionita, A. M. Pandele, L. E. Crica, and A. C. Obreja, High Perform. Polym.**28**, 181-188(2015)
49. F. Bayram Sarıipek, Int. J. Biol. Macromol.**256**, (2024)
50. K. S. Suhas, V. K. Reddy, T. Reddy, and Y. Pai, Discover Materials.**6**, 6:4(2025)
51. J.-L. Wen, Y.-Q. Ming, A.-F. Zhang, J.-L. Li, X.-Y. Du, L. Shuai, and Y.-J. Nie, Chin. J. Polym. Sci.**42**, 2069-2080(2024)
52. Y.-L. Ji, M.-J. Yin, Q.-F. An, and C.-J. Gao, Fundamental Research.**2**, 254-267(2022)
53. M. Bilal Khan, Academic Journal of Polymer Science.**1**, (2018)
54. N. Puszczykowska, P. Rytlewski, M. Macko, K. Fiedurek, and K. Janczak, Environments.**9**, 56(2022)
55. International Journal of Engineering.**31**, (2018)
56. M. Chen, C. Ma, C. Zhou, Z. Li, and R. Li, Fibers Polym.**24**, 3821–3832(2023)
57. D. R. a. T. Matsuura, Chem. Rev.**110**, 2448–2471(2010)
58. Y. Li, M. Toscano, G. Mazzone, and N. Russo, New J. Chem.**42**, 12698-12705(2018)
59. A. H. Khan, S. Hassan, M. Aamir, M. W. Khan, F. Haq, J. Hayat, M. Rizwan, A. Ullah, I. Ullah, G. Zengin, and A. Farid, Chemistry & Biodiversity.**20**, e202301068 (2023)
60. Y. Boulmokh, K. Belguidoum, F. Meddour, and H. Amira-Guebailia, (2023)

61. M. Lozada-García, R. Enríquez, T. Ramírez-Apán, A. Nieto-Camacho, J. Palacios-Espinosa, Z. Custodio-Galván, O. Soria-Arteche, and J. Pérez-Villanueva, Molecules.**22**, 633(2017)
62. T. F. Alves, M. V. Chaud, D. Grotto, A. F. Jozala, R. Pandit, M. Rai, and C. A. dos Santos, AAPS PharmSciTech.**19**, 225-231(2017)